Journal Name

ARTICLE TYPE

Cite this: DOI: 00.0000/xxxxxxxxxx

D-A$_3$ TADF Emitters: The Role of the Density of States for Achieving Faster Triplet Harvesting Rates†

Julien Eng,[a], Jerry Hagon[a] and Thomas James Penfold,[a‡]

Received Date
Accepted Date

DOI: 00.0000/xxxxxxxxxx

The triplet harvesting rate in purely organic materials based upon Thermally Activated Delayed Fluorescence (TADF) is critically important for achieving high performance Organic Light Emitting Diodes (OLEDs). One of the major challenges that must be overcome in these materials is the weak spin orbit coupling which can lead to triplet harvesting rates that extend into the millisecond range. This causes poor roll-off in device efficiency at higher current densities. In this work, we study the excited state properties of a new TADF design strategy based upon the D-A$_3$ approach. Using **TAT-3DBTO$_2$**, composed of a rigid triazatruxene donor core with three dibenzothiophene-S,S-dioxide peripheral acceptors, we explain how exploiting the high density of excited states and low lying conical intersections associated with this structure can achieve high-rates of triplet harvesting. However, we also demonstrate that excited state structural changes reduce the symmetry of the molecule and work against high triplet harvesting rates by causing localisation of the excited state electronic structure and non-equivalence between the acceptors. Consequently, the fast initial reverse intersystem crossing (rISC) channels are replaced by undesirable slower rISC channels. Our results imply that it will be possible to engineer molecules where undesirable decay pathways are removed giving new perspectives for designing functional TADF molecules.

1 Introduction

Thermally Activated Delayed Fluorescence (TADF)[1–6] offers an alternative to rare elements such as iridium[7], for harvesting triplet excited states in Organic Light Emitting Diodes (OLEDs). Importantly, high-performance devices require short emission decay times, $\sim 1\mu$s, which emphasises the importance of achieving a large rate of reverse intersystem crossing (k_{rISC})[8]. This is required to convert the 75% of non-emissive triplet states formed upon electrical excitation into emissive singlet states, as rapid k_{rISC} reduces the effect of quenching effects, such as triplet-triplet annihilation and triplet-polaron quenching[9]. Consequently there has been a significant research effort in establishing the factors which control k_{rISC} including; the energy gap[10,11], molecular conformation[12–16], presence of hetero atoms[17,18], spin-vibronic interactions[19–23] and the host[24–28].

The rate of intersystem crossing (ISC) between one singlet and triplet state can be described using Fermi's Golden Rule[29]:

$$k_{ISC} = \frac{2\pi}{\hbar}\sum_f \left|\left\langle \Psi_f \left| \hat{\mathscr{H}}_{SO} \right| \Psi_i \right\rangle\right|^2 \delta\left(E_f - E_i\right). \quad (1)$$

Within the Condon approximation, i.e. the coupling connecting the two states is constant for all geometries, the electronic and vibrational wavefunctions can be separated into:

$$k_{ISC} = \frac{2\pi}{\hbar}\sum_f \overbrace{\left|\left\langle \psi_f \left| \hat{\mathscr{H}}_{SO} \right| \psi_i \right\rangle\right|^2_{q_0}}^{\text{Electronic}} \overbrace{\sum_{jk}\left|\left\langle \nu_{fk} | \nu_{ij} \right\rangle\right|^2}^{\text{Vibrational}} \delta(E_{ij} - E_{fk}), \quad (2)$$

where $\hat{\mathscr{H}}_{SO}$ is the spin-orbit coupling operator and ψ and ν are the electronic and vibrational wavefunctions, respectively.

Equation 2 highlights the variables which can be manipulated to improve k_{ISC}. Most obviously, the spin-orbit coupling matrix elements (SOCMEs) need to be enhanced which can be achieved by exploiting heavier elements such as the transition metals[30–32]. However in the context of purely organic TADF molecules, the absence of the heavy elements places an upper limit of how large SOC can be, with the largest SOCMEs for TADF molecules reported between 3-4 cm^{-1} [20]. The second is the overlap between the vibrational wavefunctions, which is commonly achieved by reducing the energy gap between the two states, already an objective within the design of TADF emitters. The final approach, yet to be widely investigated, is to increase the number of final states (density of coupled states), indicated by the sum over f states observed in Equation 2, and which equates to increasing the rate by increasing the number of available pathways for ISC/rISC.

The role of the density of states and its ability to speed up

[a] Chemistry, School of Natural and Environmental Sciences, Newcastle University, Newcastle Upon Tyne, United Kingdom. Tel: +44 (0) 191 208 6924; E-mail: tom.penfold@newcastle.ac.uk

† Electronic Supplementary Information (ESI) available: [details of any supplementary information available should be included here]. See DOI: 00.0000/00000000.

the transitions between different spin states, is perhaps best illustrated in the ISC of Fe(II)tris(2,2'-bipyridine), $[Fe(bpy)_3]^{2+}$ [33–36]. Despite ISC being usually considered to be one of the slowest radiationless relaxation pathways, in $[Fe(bpy)_3]^{2+}$ the transfer of population from the singlet state to the quintet state, i.e. two intersystem events (singlet→triplet→quintet) occurs within 50 fs, approximately the time of a single vibrational period of the Fe-N bond length [37] and faster than many spin-allowed internal conversion events. This extremely rapid ISC, which occurs in the absence of very heavy elements such as Ir and Pt, arises because the metal-ligand charge transfer (MLCT) and metal-centred states on the iron coincide at the Franck-Condon geometry leading to a very high density of states. This illustrates a radically different regime of ISC to the usual interactions between one singlet and triplet state [29], and one in which the traditional classification of states as singlets and triplets breakdowns due to their highly mixed nature.

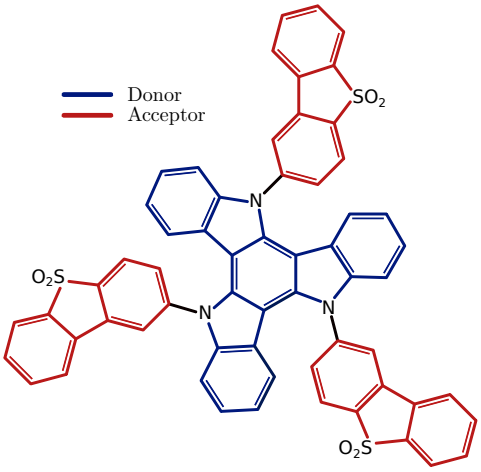

Fig. 1 Schematic of **TAT-3DBTO$_2$**. In blue, is the central triazatruxene core (TAT) and in red are the three dibenzothiophene-S,S-dioxide acceptors.

In purely organic TADF, molecular design has been dominated by D-A and D-A-D strategies [4]. While D-A-D molecules in principle have a higher density of excited states, the photophysics of molecules containing the same D and A groups is usually similar. This is because the excited state potential often leads to inequivalence in the D-A bond lengths of the D-A-D molecules. Consequently, the lower excited states which are associated with the largest D-A bond length generates an energetic landscape similar to the D-A molecules. The Franck-Condon profiles at the relaxed excited state geometry of the two molecules are therefore often similar [38]. This highlights the importance of excited state dynamics in determining the performance of TADF emitters.

Recently, dos Santos *et al.* [39] proposed a D-A_3 strategy, based upon a rigid triazatruxene donor core with three dibenzothiophene-S,S-dioxide peripheral acceptors (See Figure 1). The multiple donor-acceptor interactions yield a high density of excited states, which has been proposed to give a significant enhancement to the rISC rate, leading to delayed fluorescence decay times as low as ∼100 ns. Importantly, this demonstrates that organic molecules can harvest triplet excited states at faster rates than Ir-based phosphorescent materials. In this work, we provide a detailed theoretical study to explain how the high density of excited states and low lying conical intersections associated with this molecule can achieve these higher rates of triplet harvesting. We also demonstrate that excited state dynamics cause localisation of the excited state electronic structure, which is responsible replacing the fast initial rISC channels with slower secondary rISC channels, in which the rISC rates is analogous to typical D-A and D-A-D molecules.

2 Methods

2.1 Computational Details

All geometry optimisations and electronic structure calculations were performed within the Q-Chem 5.0 quantum chemistry package [40]. Geometries of the **TAT-3DBTO$_2$** molecule (Figure 1 and Tables S1-4 in the supporting materials) were optimised using density functional theory (DFT) and linear response time-dependent DFT (LR-TDDFT) for the ground state and excited states, respectively. The minimum energy crossing point was found and optimized using the branching-plane updating method developed by Morokuma and co-workers [41] as implemented in Q-Chem [42]. All LR-TDDFT calculations used the Tamm-Dancoff approximation [43] to avoid over stabilisation of the low lying intra-ligand triplet states. All calculations were performed within the approximation of the LRC-ωPBEh($\omega = 0.131 a_0^{-1}$) functional [44]. The value of the range separation parameter ω has been determined using the optimal tuning approach [45–48]. The 6-31G* basis set is used throughout [49–51]. All calculations included the solvent environment was described using a conductor-like polarisable continuum model using the dielectric constant of toluene. Spin-orbit couplings are computed using the one-electron Breit-Pauli Hamiltonian as implemented in Q-Chem [40]. *Ab initio* molecular dynamics (AIMD) were performed using the TeraChem [52] software using DFT in the electronic ground state, and LR-TDDFT in the excited S_1 state. Throughout the PBE functional [53,54] and 3-21G* basis set [55,56] were used. The trajectory was propagated using the velocity Verlet algorithm [57].

The absorption and emission spectra calculated from the AIMD trajectories were obtained by averaging the spectra calculated from 33 conformations taken randomly along the ground and excited state trajectories, respectively. The oscillator strength of each transition (f_n) at energy ω_n was broadened using a gaussian broadening function:

$$g(\omega - \omega_n) = \sqrt{\frac{2}{\pi\Delta^2}} \exp \frac{-2(\omega - \omega_n)^2}{\Delta^2} \quad (3)$$

where Δ is the full width at half maximum set to 10 cm^{-1} for the absorption spectrum and 20 cm^{-1} for the emission spectrum.

k_{ISC} was simulated using the Fermi's golden rule combined with a Marcus formalism to estimate the Franck-Condon weighted density of states:

$$k_{ISC} = \frac{2\pi}{\hbar} \sum_f \left| \langle \psi_f \left| \hat{\mathscr{H}}_{SO} \right| \psi_i \rangle \right|^2 \sqrt{\frac{\pi}{\lambda k_b T}} exp\left(-\frac{(\Delta E_{ST} + \lambda)^2}{4\lambda k_b T} \right) \quad (4)$$

Here λ corresponds to the reorganisation energy, which is the change in the energy of the final state when switching from the singlet to triplet geometry, while ΔE_{ST} is the energy gap between the two states.

2.2 Coordinates

To describe the excited state structural changes involved in **TAT-3DBTO$_2$** we introduce three coordinates, shown in Figure 2, describing the relative motion of each acceptor i with respect to the central donor part: (i) the torsional angle (φ_i) around the C_3-N bond, (ii) the pyramidalisation angles (τ_i) of the nitrogen and (iii) the C_3-N bond distances, r_{CN_i}. The subscript i indexes the acceptor from 1 to 3. To ensure that τ_i and φ_i are uncoupled dimensions, τ_i is defined as the dihedral angle between the planes (X_2X_1N) and (X_2NC_3) where X_1 is a dummy atom such as $\vec{OX_1} = \vec{ON} + \frac{1}{2}\vec{C_1C_3}$, O being the origin of the referential, and X_2 is a second dummy atom defined as $\vec{OX_2} = \vec{ON} + \vec{NC_1} \times \vec{NC_2}$, i.e. the $\vec{NX_2}$ vector is orthogonal to the (C_1NC_2) plane. In this picture, φ_i is the dihedral angle between the planes (C_4C_3N) and (C_3NX_2).

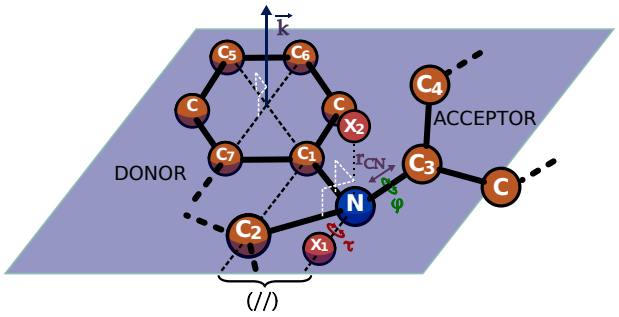

Fig. 2 Definition of the coordinates φ, τ and r_{CN} describing the conformation of each acceptor ligands. τ_i and ϕ_i are defined from -90 to 90 degrees. The purple square represents the plane of the donor group.

The final set of three dimensions, κ_i, are added to describe the distortion from planar of each of the phenyl ring at the outside end of the donor branches. κ_i is defined as the scalar product of vector $\vec{k}_i$ at each time t with itself at t=0: $\kappa_i = \vec{k}_{t=0_i}.\vec{k}_{t_i}$ where $\vec{k}(i)$ is the normal vector to the phenyl ring at the outside end of the donor branch i and is defined as the vector product $\vec{k}_i = \frac{\vec{C_1C_5}}{||\vec{C_1C_5}||} \times \frac{\vec{C_6C_7}}{||\vec{C_6C_7}||}$.

2.3 Excited State Reaction Coordinates

Potential energy scans have been performed along manually defined reaction coordinates that link key structures on the excited state potential. For each scan, the acceptor undergoing the largest amplitude motion is defined as acceptor 1. In all cases, the motion of the two other acceptors is small. Consequently, the molecule is divided into two parts: the first part (A) contains acceptors 2 and 3 as well as the donor moiety, and the second part (B) contains acceptor 1 only.

For an initial structure, α, and final structure β, each geometry is fully described by three sets of coordinates: $q_A^{\alpha,\beta}$, $q_B^{\alpha,\beta}$, the Cartesian coordinates of part A and B, respectively, and the set $\left\{\varphi^{\alpha,\beta}, \tau^{\alpha,\beta}, r_{CN}^{\alpha,\beta}\right\}$ that describes the relative position of part A with respect to part B. Distortions within A and B being small, a linear interpolation is sufficient. Therefore the coordinates of part A can be expressed as a function of the reaction coordinate r as:

$$q_A(r) = q_A^\alpha + \left(q_A^\beta - q_A^\alpha\right) r, r \in [0;1] \quad (5)$$

The set of coordinates for B, $q_B^{'\beta}$ is obtained by rotation and translation of q_B^β:

$$q_B^{'\beta} = \mathbf{R}_\varphi \mathbf{R}_\tau \left(q_B^\beta - \Delta r_{CN}\right). \quad (6)$$

The coordinates of B along the reaction coordinate r is thus:

$$q_B(r) = q_B^\alpha + \left(q_B^{'\beta} - q_B^\alpha\right) r, r \in [0;1]. \quad (7)$$

The relative motions φ, τ, and r_{CN} are then simply linearly interpolated between their initial and final values

$$\varphi(r) = \varphi^\alpha + \left(\varphi^\beta - \varphi^\alpha\right) r, r \in [0;1]. \quad (8)$$

$$\tau(r) = \tau^\alpha + \left(\tau^\beta - \tau^\alpha\right) r, r \in [0;1]. \quad (9)$$

$$r_{CN}(r) = r_{CN}^\alpha + \left(r_{CN}^\beta - r_{CN}^\alpha\right) r, r \in [0;1]. \quad (10)$$

This treatment ensures that there is no artificially large distortion of the acceptor 1 due to a poor treatment of its rotations. However this interpolation cannot account for the order in which the distortions would occur. These coordinates therefore do not describe the minimum energy pathway between two critical structures.

3 Results

3.1 Geometry

In previous work[39], 10 different conformations of **TAT-3DBTO$_2$** were identified, but shown to have negligible effect on the energy and character of the low lying excited states. Consequently, we focus this present study on the dominant **TAT-3DBTO$_2$** conformer[39] exhibiting C_3 symmetry.

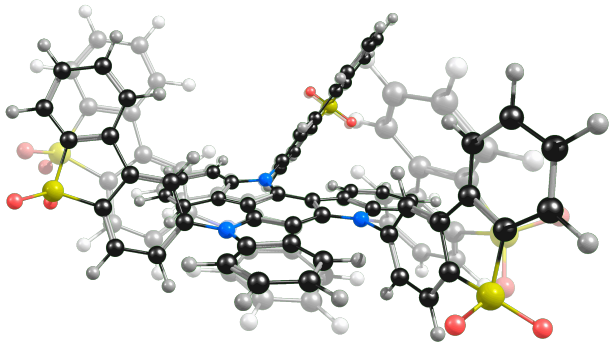

Fig. 3 A comparison between the ground (faded) and excited S_1 (coloured) geometries of **TAT-3DBTO$_2$**.

Table 1 shows the geometry of **TAT-3DBTO$_2$** at the ground state, the optimised S_1 and T_1 geometries and the conical intersection

	FC	S_1	CI^{S_1/S_2}	T_1
$\varphi_1/^\circ$	-33.69	-15.67	-12.81	29.04
$\varphi_2/^\circ$	-33.69	-29.21	-21.14	-26.98
$\varphi_3/^\circ$	-33.69	-28.31	-32.22	-39.30
$\tau_1/^\circ$	16.12	3.89	1.72	-16.17
$\tau_2/^\circ$	16.12	16.95	6.20	18.37
$\tau_3/^\circ$	16.12	14.96	13.38	14.30
r_{CN_1}/Å	1.411	1.432	1.432	1.415
r_{CN_2}/Å	1.411	1.419	1.421	1.416
r_{CN_3}/Å	1.411	1.420	1.418	1.406

Table 1 The structural parameters for the structure of **TAT-3DBTO$_2$** at the ground state Franck-Condon (FC) geometry, the minimum of S_1 and T_1 states and the conical intersection between S_1 and S_2 (CI^{S_1/S_2}).

formed between the S_1 and S_2 states. The cartesian coordinates for these structures are provided Tables S1-4. A comparison between the ground and S_1 excited geometries is shown in Figure 3. All geometries are described exclusively using the three coordinates, φ_i, τ_i and r_{CN_i} described above. The conical intersection is formed because the S_1 and S_2 consists of predominately HOMO→LUMO and HOMO-1→LUMO transitions, respectively. Both the HOMO and HOMO-1 are π orbitals localised on the donor unit of **TAT-3DBTO$_2$** and describe two different conformations of the π-system, which can become degenerate at the midpoint of this geometry.

In the ground state, the torsional angle (φ_i) is -34° with respect to perpendicular with the donor moiety, which is in good agreement with the X-ray structure measured experimentally[39]. The C-N bridges between the acceptor and donor units are out of the donor plane by an angle of $\tau = 16.12^\circ$ with a C-N bond distance of $r_{CN} = 1.41$ Å. The excited state (S_1 and CI^{S_1/S_2}) structures exhibit clear breaking of the C_3 symmetry observed in the ground state with the largest changes observed for one of the acceptors. This is consistent with localisation of the excited charge transfer state to occur between the donor and one acceptor and is discussed in more detail in the following. For this acceptor the torsional angle (φ_i) becomes closer to perpendicular, and more in the plane of the donor, as illustrated by the reduction in τ_1. There is a slight elongation of r_{CN} for this acceptor, which although small, has a strong effect on the excited charge transfer states due to the 1/R dependence of these excitations, where R is the distance between donor and acceptor groups[25].

Figure 4 shows the distribution of the angles φ and τ as well as the donor-acceptor bond length r_{CN} obtained from 10 ps of AIMD propagated in the electronic ground state. Although similar, it is noted that due to the different level of theory used for the AIMD compared to the results in Table 1, direct quantitative comparison is not possible. φ_1 and φ_2 shows a quasi-normal distribution around an average value of $\langle\varphi_1\rangle = -32.84^\circ$ and $\langle\varphi_2\rangle = -33.92^\circ$, respectively. The asymmetry in the distribution of φ_1 and φ_2 is due to the steric hindrance between the acceptor units and the neighbouring donor branches for values of $\varphi < -50^\circ$. Acceptor 3 explores a wider region of the multidimensional ground state potential and the two peaks in the distribution reflect the two minima can be found on the ground states PES around $\varphi_3 = -45^\circ$ and $\varphi_3 = -10^\circ$, respectively[39]. The pyramidalisation angle (τ) of each nitrogen atom and the donor-acceptor bond lengths (r_{CN}) all exhibit similar behaviour for each acceptor.

The excited state distributions (white boxes in Figure 4) exhibit the same effect of symmetry breaking associated with charge localisation observed in Table 1. The elongation of the D-A only occurs for r_{CN_1}, while the other D-A bond distances remain similar to the ground state. An overall opening of the system, i.e. the C-N bond aligning into the donor plane, is observed as the distribution of τ_1, τ_2 and τ_3 are shifted to smaller values. This opening of the C-N bonds allow for the acceptors to rotate further, leading to a broader distribution of φ_2 and φ_3. φ_1 becomes close to an orthogonal arrangement between the donor and acceptors groups and its distribution is slightly smaller as it is held place by being involved in the charge transfer (CT) excitation.

3.2 Critical Points on the Potential Energy Surface

3.2.1 The Electronic Ground State and Absorption Spectrum

Figure 5 shows the computed absorption spectrum at the optimised structure of the electronic ground state (blue line) overlaid against the experimental spectrum (grey line). The band between 300-350 nm corresponds to a weak absorption band associated with CT states. In agreement with the experimental spectrum[39], two peaks at higher energy, around 270 and 220nm, are observed. The higher intensity of these absorption bands is because of: (i) the higher density of singlet states and (ii) mixing between ^{1}CT and locally excited (^{1}LE) states, with the latter providing oscillator strength to the transitions. As shown in ref.[39], these two peaks can be approximated from the absorption spectrum of the donor and acceptor moieties confirming the LE character of these transitions.

Table 2 shows the states that fall within the first low energy CT absorption band < 3.70 eV (< 335nm). The difference of electronic density associated with each excited state is shown in Figure 6. The lowest ^{1}CT singlet states are at $E_{S_1} = 3.61$ eV and $E_{S_2} = 3.66$ eV. The corresponding ^{3}CT triplet states are at lower energy and are heavily mixed with triplet local excitons (^{3}LE) on either the donor or the acceptor units. Seven triplet states of mixed character are found between 3.09 and 3.51 eV.

As shown in Figure 6, the difference of electronic density associated with each excited state is delocalised over the whole molecule in nearly all cases, with the exception of states which show strong mixing with the LE states. In these cases the delocalisation only occurs over two of the acceptors.

The absorption spectrum calculated at the Franck-Condon geometry (Figure 5) offers good agreement with the experimental spectrum, although the CT band is slightly too narrow. To assess the effect of the geometry distributions occurring at finite temperature illustrated in Figure 4, an absorption spectrum was calculated by averaging 33 snapshots geometries taken randomly along the MD trajectory and is shown in Figure 5 (red line). The averaging over several structures improves the agreement between experimental and calculated spectrum, principally through broadening the low-lying CT band. As expected this has little effect on the higher lying excited states which are dominated by

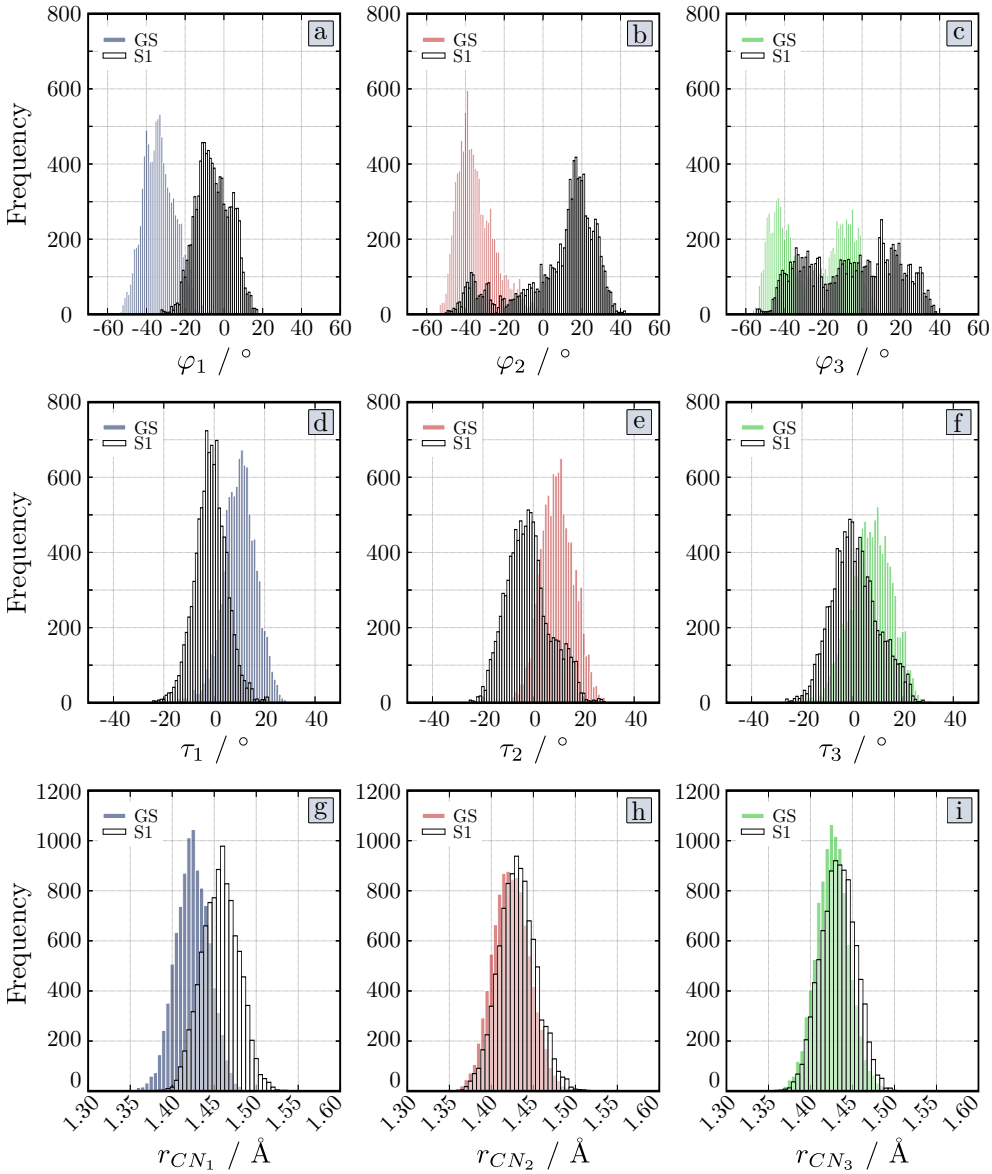

Fig. 4 The distribution of a) φ_1, b) φ_2, c) φ_3, d) τ_1, e) τ_2, f) τ_3 and g) r_{CN_1} e) r_{CN_2} h) r_{CN_3} along the trajectory in both the ground state (coloured boxes) and S_1 (white boxes).

LE character. Table S6 shows the spin-orbit coupling matrix elements (SOCMEs) between the lowest singlet and triplet excited states at the ground state optimised geometry. SOCMEs are weak, $< 1\text{cm}^{-1}$ in most cases, as expected in organic molecules.

3.2.2 The Excited S_1 State and the Emission Spectrum

Table 3 shows the excited states of **TAT-3DBTO$_2$** at the minimum of S_1. The geometry at this point, as previously discussed (Table 1) differs mainly from the ground state in the orientation of one of the acceptors. At the minimum of the S_1 potential energy surface, the electronic nature of the lowest excited singlet state is a pure HOMO→LUMO charge transfer transition localised on only one acceptor. The minimum of S_1 lies at E_{S1}=2.89 eV, corresponding to an emission wavelength of λ^{em} = 429nm and a Stokes shift in S_1 of $E_{S_1}^{S.S.} = 0.72$ eV in agreement with experimental observations[39] as shown in Figure 5. The presence of a low-lying triplet local exciton (^{3}LE) on acceptor 1 induces a high mixing with the triplet charge transfer states. This results in a splitting of the T_1/S_1 states of ΔE=0.17 eV, with E_{T_1} 2.72 eV while T_2 is pushed above the S_1 to E_{T_2}=2.94 eV. At the S_1 minimum, the SOCME between the lowest excited states remain weak and comparable to those at Franck-Condon (Table S7).

The breaking of the symmetry associated with the excited state, discussed in the previous section which leads to the localisation of the CT on one acceptor and gives rise to an excited state potential profile where the density of state around S_1 which is much lower compared to the ground state geometry. Instead of having many possible relaxation pathways from the singlet to triplet states, it is only the $S_1 \rightarrow T_1$ and $S_1 \rightarrow T_2$ pathways, which contribute. This electronic structure resembles to the electronic structure of the previously studied D-A and D-A-D molecules[19,22,58]. Crucially

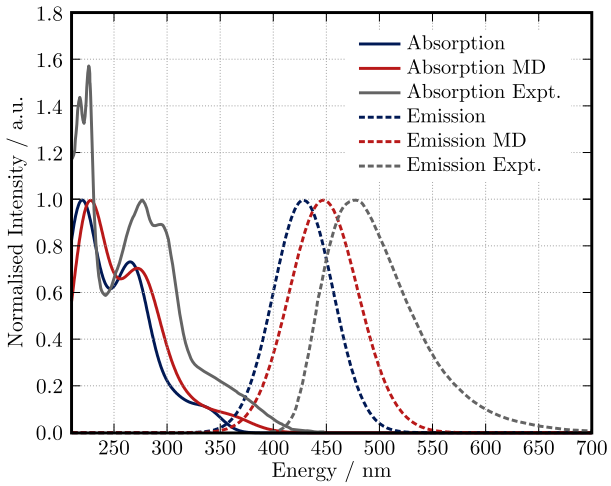

Fig. 5 The absorption (full lines) and emission (dashed lines) spectra of **TAT-3DBTO$_2$** computed at the minimum energy geometry (blue line) and averaged spectrum over 33 structures extracted from the MD simulation in the ground state at 300K (red line). The grey lines are the experimental spectra replotted from ref.[39].

this is driven by the inequivalence in D-A bond lengths, as observed for D-A and D-A-D molecules[38].

Figure 5 shows the simulated emission band calculated from sampling geometries obtained from the *ab initio* MD. Compared to the optimised geometry, this spectrum is shifted to $\lambda^{em} =$ 450nm, slightly shorter than found in the experiment. The asymmetry of the emission band is also partly recovered, which is associated with anharmonicity in the excited state potential.

Table 1 shows that the relaxed T_1 state exhibits the largest change in the pyramidalisation (τ) angle, i.e. the most open structure of the acceptor with respect to the donor. Importantly, as with other TADF emitters[19–22], the lowest triplet state is a locally excited state on the acceptor, which is consistent with the vibronic structure observed in the phosphorescence spectrum at low temperature[39]. The energy of the T_1 state at this geometry is 2.45 eV (Table S5) in very close agreement with the peak of the phosphorescence spectrum of 500 nm reported experimentally[39].

3.2.3 The S_1-S_2 conical intersection

The high density of excited states associated with **TAT-3DBTO$_2$** increases the probability of crossings and conical intersections between the states of the same multiplicity. These topological features are well known to provide very efficient pathways for radiationless conversion between states[59], and therefore could facilitate rapid rISC. As discussed above, **TAT-3DBTO$_2$** exhibits a low lying conical intersection, which arises from a degeneracy formed between orbitals on the donor.

Table 4 shows the electronic structure at the minimum of the seam of conical intersection. The S_1 and S_2 are degenerate at 3.07eV and are of mixed HOMO→LUMO and HOMO-1→LUMO character. This is 0.16 eV higher than the minimum energy geometry of the S_1 state. At this geometry, the overlap between the HOMO and LUMO and between the HOMO-1 and LUMO is close to 0 and therefore the ^3CT states associated to S_1 and S_2 could

State	Nature	f	Δ E / eV
S_0		-	0.00
T_1	^{3}LE(D)/^{3}CT	-	3.09
T_2	^{3}CT/^{3}LE(A)	-	3.18
T_3	^{3}CT/^{3}LE(A)	-	3.18
T_4	^{3}CT/^{3}LE(D)/^{3}LE(A)	-	3.23
T_5	^{3}LE(D)/^{3}CT	-	3.42
T_6	^{3}LE(D)/^{3}CT	-	3.42
T_7	^{3}LE(D)/^{3}CT	-	3.51
S_1	^{1}CT	0.005	3.61
T_8	^{3}CT/^{3}LE(A)	-	3.66
T_9	^{3}CT/^{3}LE(A)	-	3.66
S_2	^{1}CT	0.175	3.66
T_{10}	^{3}CT/^{3}LE(A)	-	3.67
S_3	^{1}CT	0.183	3.67
S_4	^{1}CT	0.005	3.73

Table 2 Energy, nature and oscillator strength (f) of the lowest singlet and triplet excited states at the Franck-Condon geometry. CT denotes a charge transfer from the donor (D) to the acceptor (A) and LE(A), LE(D) are local excitons on the acceptor and donor, respectively.

State	Nature	f	Δ E / eV
S_0		-	0.41
T_1	^{3}CT/^{3}LE(A)	-	3.13
S_1	^{1}CT	0.004	3.30
T_2	^{3}CT/^{3}LE(D)/^{3}LE(A)	-	3.35
T_3	^{3}CT/^{3}LE(D)/^{3}LE(A)	-	3.44
T_4	^{3}LE(D)/^{3}CT	-	3.59
T_5	^{3}LE(D)/^{3}CT	-	3.61
T_6	^{3}CT	-	3.64
S_2	^{1}CT	0.012	3.67
T_7	^{3}CT/^{3}LE(D)	-	3.75

Table 3 Energy, nature and oscillator strength (f) of the lowest singlet and triplet excited states at the geometry of the minimum of S_1 excited state with LRC-ωPBEh ($\omega = 0.131 a_0^{-1}$). CT denotes a charge transfer from the donor (D) to one or several acceptors (A), and LE(A), LE(D) are local excitons on one or several acceptors and donor, respectively. All Energies are relative to the energy of the ground state at the Franck-Condon Geometry.

be expected to be degenerate and lying close to the pair of degenerate state S_1 and S_2[45]. This would generate a point in which many states and different multiplicity cross, with the potential of enhancing ISC/rISC. However, the presence of a low lying ^{3}LE states split the degeneracy between the pair of ^3CT states. The first triplet T_1 at E_{T_1}=2.77 eV is a mix of LE and CT character, with LE being the main contribution. T_2 and T_3 lie at 3.03 eV and 3.09 eV respectively and are of quasi pure ^{3}CT character and therefore are close in energy to the pair of ^{1}CT states (ΔE = 0.03 eV).

The spin-orbit coupling matrix elements associated with this geometry are shown in Table S9 and are not enlarged, compared to the optimised ground and S_1 excited state, illustrating consistent with previous work[60] that the conical intersection does not necessarily increase SOCME as it does with nonadiabatic coupling. Although this would suggest that the ISC/rISC rate is not enhanced at this geometry, the close proximity of the S_1, S_2 and T_1, T_2 and T_3 states at this geometry will increase the effect of

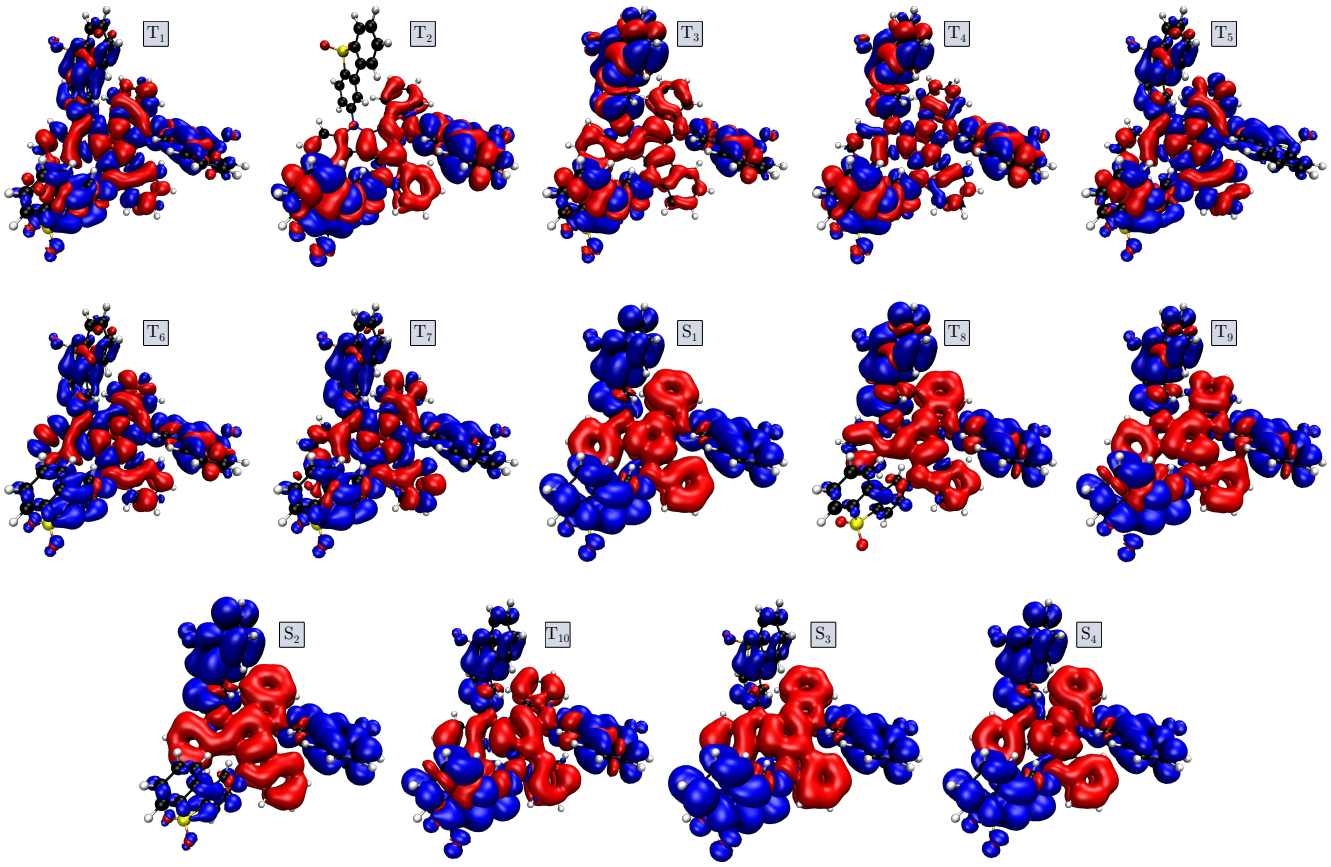

Fig. 6 Density difference between the fourteen lowest excited states and the ground state. In red: loss of density. In blue: gain.

this coupling which scales inversely with the energy gap.

3.2.4 The S_1 Reaction Pathways

After excitation into the S_1 CT excited state, **TAT-3DBTO$_2$** will undergo structural dynamics to reach the minimum of its potential energy surface. The critical points on the excited state potential have been identified in the previous sections, without dynamical information or insight into the pathways connecting these points. Figure S1 shows the evolution of the structural coordinates defined in Figure 2 along an AIMD simulation in the S_1 excited state during the first picosecond after vertical projection of the ground state geometry into the S_1 state. Initially, the charge transfer character of this S_1 state is delocalised from the donor to all three acceptor units. However, the structural changes observed within the first 200 fs already illustrate the symmetry breaking associated with localisation of the CT state. The largest changes are observed in both r_{CN_1} and φ_1. The C-N bond elongation observed in acceptor 1, unlocks its rotation which is observed with changes in τ and φ. φ_1 increases from the initial tilted geometry of $\varphi_1 = -33.69^\circ$ to $\varphi_1 = 0.00^\circ$, i.e. the acceptor is perpendicular to the donor plane. Being a low frequency mode, this happens much slower than the bond length change in about 1.0 ps. φ_2 and φ_3 remain nearly constant during that time. Additional trajectories fro different starting points sampled from the ground state molecular dynamics are shown in Figure S2-7.

To compliment the AIMD, Figure 8 shows the evolution of the lowest excited states along interpolated reaction coordinates between three critical structures presented, the ground state, S_1 state and S_1/S_2 conical intersection. The pathway from the Franck-Condon structure to the minimum of S_1 (Figure 8a) exhibits a small energy barrier of 63 meV in the S_1 state, which is consistent with the simultaneous structural changes observed in the AIMD. The energy needed to reach the conical intersection between S_1 and S_2 from the minimum of S_1 $\Delta E = 0.16$eV (Figure 8b) is smaller than the change in the energy of the S_1 during this relaxation, $\sim$0.3 eV, and therefore can easily be reached upon absorption in S_1. The direct pathway (figure 8c) from Franck-Condon to the conical intersection exhibits a barrier 0.25 eV. This suggests that geometry relaxation from the Franck-Condon geometry to the minimum of the S_1 geometry occurs first, consistent with the observations of the AIMD. At later times, the vibrational excess energy enable the molecule to sample regions of the potential close to the conical intersection. This confirms that the critical points identified can all be reach by the initial excitation into the S_1 state and will therefore play a role in the photophysics of **TAT-3DBTO$_2$**.

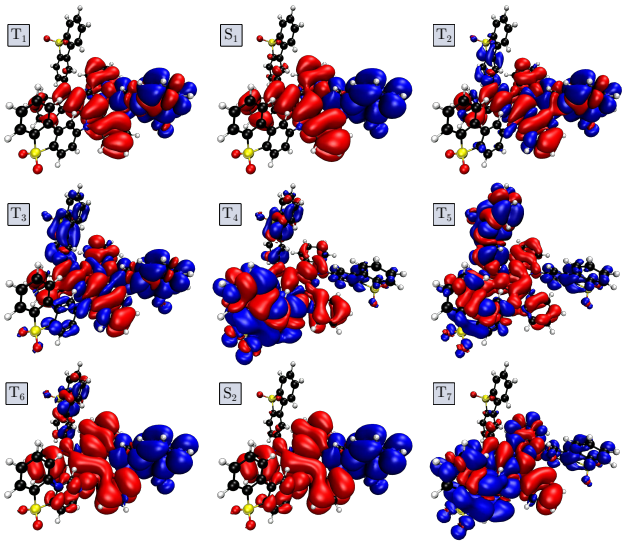

Fig. 7 Density difference between the nine lowest excited states and the ground state at the S_1 optimised geometry. In red: loss of density. In blue: gain. These plots show the strong localisation of the CT states, associated with the structural changes observed with respect to the ground state geometry.

State	Nature	f	Δ E / eV
S_0		-	0.39
T_1	^{3}LE(A)	-	3.16
T_2	^{3}CT/^{3}LE(D)	-	3.42
S_1	^{1}CT	0.004	3.46
S_2	^{1}CT	0.009	3.46
T_3	^{3}CT/^{3}LE(D)	-	3.48
T_4	^{3}CT	-	3.50
T_5	^{3}CT/^{3}LE(A)	-	3.56
T_6	^{3}CT/^{3}LE(A)/^{3}LE(D)	-	3.60
T_7	^{3}CT/^{3}LE(D)	-	3.74
T_8	^{3}CT/^{3}LE(D)/^{3}LE(A)	-	0.81
S_3	^{1}CT	0.031	3.83
S_4	^{1}CT	0.045	3.85

Table 4 Energy, nature and oscillator strength (f) of the lowest singlet and triplet excited states at the geometry of the conical intersection between S_1 and S_2, with LRC-ωPBEh ($\omega = 0.131 a_0^{-1}$). CT denotes a charge transfer from the donor (D) to one or several acceptors (A), and LE(A), LE(D) are local excitons on one or several acceptors and donor, respectively. All Energies are relative to the energy of the ground state at the Franck-Condon Geometry.

3.2.5 ISC and rISC rates

The experimentally[39] reported k_{ISC} =3.5×10^7 s^{-1} for **TAT-3DBTO$_2$** means that ISC occurs on the nanosecond timescale. This rate of ISC is fairly typical of higher performing TADF molecules, although rates approaching 10^9 s^{-1} have been observed for molecules exhibit room-temperature phosphorescence[14] and molecules such as benzophenone have shown k_{ISC}=10^{10-11} s^{-1}[61].

Table 5 shows the k_{ISC} calculated at two critical geometries, the S_1 minimum and the S_1-S_2 conical intersection. For the former, a rate of $6.3\times 10^7 s^{-1}$ is calculated. At the conical intersection, an order of magnitude increase in the ISC rate is observed, with a singlet→triplet rate being $3.0\times 10^8 s^{-1}$. The enhancement in the region of the conical intersection is associated with the close proximity of the states, and the increased number of pathways, i.e. density of states.

Both pathways provide good agreement with experimentally observed, but importantly at the conical intersection geometry the k_{rISC} would be equal to k_{ISC}, because the energy gap between the singlet and triplets is very small (Table 5), this is consistent with the fast k_{rISC} observed on the nanosecond timescale in ref.[39]. However, once the k_{ISC} is complete, the molecule will relax into the lowest triplet state. This will result in the fast initial k_{rISC} channel being replaced by undesirable slower secondary k_{rISC} channels, due to the T_1 state is lying substantially below the higher triplet states and the S_1 state, providing a rationalisation for a k_{rISC} which reduces with time.[39].

It is noted that it can be argued whether or not the Fermi golden rule can be used to calculate the rate constants in the region of a conical intersection, where the concept of first order perturbation theory breakdowns down. Indeed, although similar approaches have been used elsewhere[62] the approach described herein should only be taken as an approximation of the ISC/rISC dynamics. A more precise description should include nonadiabatic effects and excited state dynamics, but the size of system and timescale of the dynamics prevents this at present.

4 Discussion and Conclusions

In this paper we have performed a detailed theoretical investigation into the excited state properties of a TADF emitter exploiting the recently proposed D-A_3 strategy[39]. **TAT-3DBTO$_2$**, which is based upon a rigid triazatruxene donor core with three dibenzothiophene-S,S-dioxide peripheral acceptors, has demonstrated that rapid rISC rate can be achieved in purely organic molecules leadings to delayed fluorescence decay times as low as ∼100 ns. Our simulations show that upon initial photoexcitation of the low lying ^{1}CT state, the electron transferred is delocalised over the acceptor units. This leads to a number of close lying excited states and multiple degeneracies which can enhance the mixing between singlet and triplet states.

However, structural changes occurring within the first picosecond introduce a breaking of the coordination symmetry causing localisation of the photoexcited electron onto one of the acceptors. Within this regime, the excited state can be seen as analogous to a D-A molecule and indeed the k_{rISC} observed at later times is consistent with this[39]. This is analogous to the origin of the similarities between the photophysics between D-A and D-A-D molecules containing the same D and A groups. In theses cases, the excited state potential often leads to inequivalence in D-A bond lengths of the D-A-D complexes, and therefore the lower excited states, associated with the largest D-A bond length generates an energetic landscape similar to the D-A molecules. The Franck-Condon profiles at the relaxed excited state geometry of the two molecules are therefore often similar[38].

Recently de Silva et al.[63] proposed a four state model for TADF

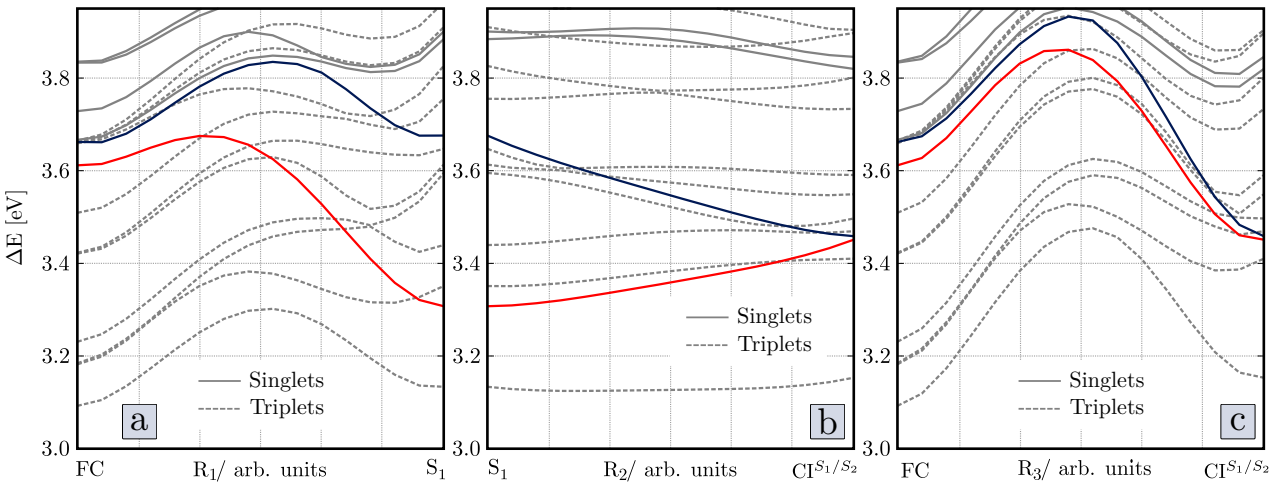

Fig. 8 Energy scan a) from the ground state optimised Franck-Condon geometry to the geometry of the minimum of S_1 b) from the geometry of the minimum of S_1 to the S_1/S_2 conical intersection, and c) from the ground state optimised geometry to the S_1/S_2 conical intersection. The reaction path has been simulated by a linear interpolation between the initial and final geometries. Details about the reaction coordinates can be found in section 2.3. The red line is the S_1 state, the blue line is the S_2 state, the grey dashed lines are triplet states and the grey solid lines are other singlet states.

	SOCME cm^{-1}	λ eV	ΔE_{ST} eV	k_{ISC} $\times 10^7 s^{-1}$
S_1 Min.				
S_1-T_1	0.645	0.31	-0.17	5.80
S_1-T_2	0.610	0.39	0.05	0.51
				6.31
S_1-S_2 CI				
S_1-T_1	0.880	0.31	-0.30	20.05
S_1-T_2	0.702	0.39	-0.04	0.53
S_1-T_3	0.946	0.35	0.02	4.52
S_1-T_4	0.466	0.35	0.04	0.72
S_2-T_1	0.277	0.31	-0.30	1.53
S_2-T_2	0.759	0.39	-0.05	0.63
S_2-T_3	0.305	0.35	0.02	0.50
S_2-T_4	0.855	0.35	0.04	2.42
				30.90

Table 5 The k_{ISC} calculated using Fermi's golden rule combined with a Marcus formalism to estimate the Franck-Condon weighted density of states. The rate is calculated at two geometries, the minimum of the S_1 state and the conical intersection between the S_1-S_2 states.

emitters including the LE and CT states, building upon the spin-vibronic model in refs [19,22]. They proposed that specific conformations could be key to achieving high-performance TADF and a similar situation is observed in the present case. In the region of the Franck-Condon geometry and the conical intersection between the S_1 and S_2 states, the high density of states of **TAT-3DBTO$_2$** facilitates rapid ISC between the singlet and triplet states, while the small energy gap means the rISC occurs at a similar rate. However, excited state relaxation takes the molecule to regions of the potential which cannot exhibit such favourable rates. This is in line with the experimental observations that at later times, the rISC rate falls from an initial value of $\sim 10^7$ s^{-1} to $\sim 10^5$ s^{-1}, which suggests that relaxation in the triplet states away from the optimal conformations of the Franck-Condon geometry, the lower density of states causes a reduced rate in rISC.

This strongly indicates that the future design of TADF emitters should focus upon controlling the geometry and excited state distortions to restrict the symmetry breaking which leads to the reduced density of states leading to the slow rISC. Locking the molecules into a rigid conformation is challenging [64–66] as most TADF emitters reported to date require the molecule to vibrate and samples regions of the potential which exhibit small energy gaps and larger radiative rates. These are usually not the same geometry. The coordinates used to describe the symmetry breaking reduces the excited state structural dynamics of a large molecules into a subset of 3 coordinates. These coordinates are termed dynamo-phores, the dynamical version of a chromophore. The reframing of the excited state structural changes in this manner will facilitate the design by increasing the predictive power and enabling a modular approach that will be rational, intuitive and underpinned by strong theoretical foundations. Finally, the fastest initial rISC channel is responsible for the DF decay and, in a device context will lead to the highest external quantum efficiency in devices. The slower, late time rISC channels associated with the symmetry breaking of the excited states will likely cause

long DF and poor efficiency roll-off in devices.

Conflicts of interest

There are no conflicts to declare.

Acknowledgements

We gratefully acknowledge support from the EPSRC through Grants EP/N028511/1, EP/R021503/1, and EP/P012388/1.

Notes and references

1 H. Uoyama, K. Goushi, K. Shizu, H. Nomura and C. Adachi, *Nature*, 2012, **492**, 234–238.

2 Q. Zhang, B. Li, S. Huang, H. Nomura, H. Tanaka and C. Adachi, *Nat. Photonics*, 2014, **8**, 326.

3 H. Noda, H. Nakanotani and C. Adachi, *Sci. Adv.*, 2018, **4**, eaao6910.

4 M. Y. Wong and E. Zysman-Colman, *Adv. Mater.*, 2017, **29**, 1605444.

5 T. Penfold, F. Dias and A. Monkman, *Chem. Comm.*, 2018, **54**, 3926–3935.

6 F. B. Dias, T. J. Penfold and A. P. Monkman, *Methods Appl. Fluoresc.*, 2017, **5**, 012001.

7 D. Volz, M. Wallesch, C. Flechon, M. Danz, A. Verma, J. M. Navarro, Z. Daniel, S. Braese and T. Baumann, *Green Chem.*, 2015 **17**, 1988-2011.

8 M. Inoue, T. Serevičius, H. Nakanotani, K. Yoshida, T. Matsushima, S. Juršėnas and C. Adachi, *Chem. Phys. Lett.*, 2016, **644**, 62–67.

9 H. Yersin, *Transition Metal and Rare Earth Compounds*, Springer, 2004, 1–26.

10 Y. Sagara, K. Shizu, H. Tanaka, H. Miyazaki, K. Goushi, H. Kaji and C. Adachi, *Chem. Lett.*, 2014, **44**, 360–362.

11 J. Lee, K. Shizu, H. Tanaka, H. Nakanotani, T. Yasuda, H. Kaji and C. Adachi, *J. Mater. Chem. C*, 2015, **3**, 2175–2181.

12 K. Wang, C.-J. Zheng, W. Liu, K. Liang, Y.-Z. Shi, S.-L. Tao, C.-S. Lee, X.-M. Ou and X.-H. Zhang, *Adv. Mater.*, 2017, **29**, 1701476.

13 M. K. Etherington, F. Franchello, J. Gibson, T. Northey, J. Santos, J. S. Ward, H. F. Higginbotham, P. Data, A. Kurowska, P. L. Dos Santos *et al.*, *Nat. Comm.*, 2017, **8**, 14987.

14 R. Huang, J. S. Ward, N. A. Kukhta, J. Avó, J. Gibson, T. Penfold, J. C. Lima, A. S. Batsanov, M. N. Berberan-Santos, M. R. Bryce *et al.*, *J. Mater. Chem. C*, 2018, **6**, 9238–9247.

15 T. Matulaitis, P. Imbrasas, N. A. Kukhta, P. Baronas, T. Bučiūnas, D. Banevičius, K. Kazlauskas, J. V. Gražulevičius and S. Juršėnas, *J. Phys. Chem. C*, 2017, **121**, 23618–23625.

16 Y. Cao, J. Eng and T. J. Penfold, *J. Phys. Chem. A*, 2019, **123**, 2640-2649.

17 H. Tanaka, K. Shizu, J. Lee and C. Adachi, . *Phys. Chem. C*, 2015, **119**, 2948–2955.

18 R. Huang, J. Avó, T. Northey, E. Chaning-Pearce, P. L. dos Santos, J. S. Ward, P. Data, M. K. Etherington, M. A. Fox, T. J. Penfold *et al.*, *J. Mater. Chem. C*, 2017, **5**, 6269–6280.

19 J. Gibson, A. P. Monkman and T. J. Penfold, *ChemPhysChem*, 2016, **17**, 2956–2961.

20 C. M. Marian, *J. Phys. Chen. C*, 2016 **120**,3715-3721.

21 J.-M. Mewes, *Phys. Chem. Chem. Phys.*, 2018, **20**, 12454–12469.

22 M. K. Etherington, J. Gibson, H. F. Higginbotham, T. J. Penfold and A. P. Monkman, *Nat. Comm.*, 2016, **7**, 13680.

23 Y. Cao, J. Eng and T. Penfold, *J. Phys. Chem. C*, 2019 **123** 2640-2649.

24 P. L. dos Santos, J. S. Ward, M. R. Bryce and A. P. Monkman, *J. Phys. Chem. Lett.*, 2016, **7**, 3341–3346.

25 T. Northey, J. Stacey and T. Penfold, *J. Mater. Chem. C*, 2017, **5**, 11001–11009.

26 G. Méhes, K. Goushi, W. J. Potscavage Jr and C. Adachi, *Org. Electron*, 2014, **15**, 2027–2037.

27 M. K. Etherington, N. A. Kukhta, H. F. Higginbotham, A. Danos, A. N. Bismillah, D. R. Graves, P. R. McGonigal, N. Haase, A. Morherr, A. S. Batsanov *et al.*, *J. Phys. Chem. C*, 2019, **123** 11109-11117.

28 C. Deng, L. Zhang, D. Wang, T. Tsuboi and Q. Zhang, *Adv. Opt. Mater.*, 2019, 1801644.

29 T. Penfold, G. E, C. Daniel and C. Marian, *Chem. Rev.*, 2018, **118**, 6975-7025.

30 D. Di, A. S. Romanov, L. Yang, J. M. Richter, J. P. Rivett, S. Jones, T. H. Thomas, M. A. Jalebi, R. H. Friend, M. Linnolahti, M. Bochmann, D. Credgington *Science*, 2017, **356**, 159–163.

31 S. Thompson, J. Eng and T. Penfold, *J. Chem. Phys.*, 2018, **149**, 014304.

32 R. Hamze, J. L. Peltier, D. Sylvinson, M. Jung, J. Cardenas, R. Haiges, M. Soleilhavoup, R. Jazzar, P. I. Djurovich, G. Bertrand, M.E. Thompson *Science*, 2019, **363**, 601–606.

33 J. K. McCusker, K. N. Walda, R. C. Dunn, J. D. Simon, D. Magde and D. N. Hendrickson, *J. Am. Chem. Soc.*, 1992, **114**, 6919–6920.

34 A. Cannizzo, C. Milne, C. Consani, W. Gawelda, C. Bressler, F. Van Mourik and M. Chergui, *Coord. Chem. Rev.*, 2010, **254**, 2677–2686.

35 W. Zhang, R. Alonso-Mori, U. Bergmann, C. Bressler, M. Chollet, A. Galler, W. Gawelda, R. G. Hadt, R. W. Hartsock, T. Kroll, K. S. Kjaer, K. Kubicek, H. T. Lemke, H. W. Liang, D. A. Meyer, M. M. Nielsen, C. Purser, J. S. Robinson, E. I. Solomon, Z. Sun, D. Sokaras, T. B. van Driel, G. Vanko, T-C Weng, D Zhu and K. J. Gaffney *Nature*, 2014, **509**, 345.

36 G. Auböck and M. Chergui, *Nat. Chem.*, 2015, **7**, 629.

37 C. Bressler, C. Milne, V.-T. Pham, A. ElNahhas, R. M. van der Veen, W. Gawelda, S. Johnson, P. Beaud, D. Grolimund, M. Kaiser *et al.*, *Science*, 2009, **323**, 489–492.

38 M. Merriam, R. Rodriguez and J. L. McHale, *J. Phys. Chem.*, 1987, **91**, 1058–1063.

39 P. L. dos Santos, J. S. Ward, D. G. Congrave, A. S. Batsanov, J. Eng, J. E. Stacey, T. J. Penfold, A. P. Monkman and M. R. Bryce, *Adv. Sci.*, 2018, **5**, 1700989.

40 Y. Shao, Z. Gan, E. Epifanovsky, A. T. Gilbert, M. Wormit, J. Kussmann, A. W. Lange, A. Behn, J. Deng, X. Feng, D. Ghosh, M. Goldey, P. R. Horn, L. D. Jacobson, I. Kaliman,

R. Z. Khaliullin, T. Kuś, A. Landau, J. Liu, E. I. Proynov, Y. M. Rhee, R. M. Richard, M. A. Rohrdanz, R. P. Steele, E. J. Sundstrom, H. L. Woodcock, P. M. Zimmerman, D. Zuev, B. Albrecht, E. Alguire, B. Austin, G. J. O. Beran, Y. A. Bernard, E. Berquist, K. Brandhorst, K. B. Bravaya, S. T. Brown, D. Casanova, C.-M. Chang, Y. Chen, S. H. Chien, K. D. Closser, D. L. Crittenden, M. Diedenhofen, R. A. DiStasio, H. Do, A. D. Dutoi, R. G. Edgar, S. Fatehi, L. Fusti-Molnar, A. Ghysels, A. Golubeva-Zadorozhnaya, J. Gomes, M. W. Hanson-Heine, P. H. Harbach, A. W. Hauser, E. G. Hohenstein, Z. C. Holden, T.-C. Jagau, H. Ji, B. Kaduk, K. Khistyaev, J. Kim, J. Kim, R. A. King, P. Klunzinger, D. Kosenkov, T. Kowalczyk, C. M. Krauter, K. U. Lao, A. D. Laurent, K. V. Lawler, S. V. Levchenko, C. Y. Lin, F. Liu, E. Livshits, R. C. Lochan, A. Luenser, P. Manohar, S. F. Manzer, S.-P. Mao, N. Mardirossian, A. V. Marenich, S. A. Maurer, N. J. Mayhall, E. Neuscamman, C. M. Oana, R. Olivares-Amaya, D. P. O'Neill, J. A. Parkhill, T. M. Perrine, R. Peverati, A. Prociuk, D. R. Rehn, E. Rosta, N. J. Russ, S. M. Sharada, S. Sharma, D. W. Small, A. Sodt, T. Stein, D. StÃijck, Y.-C. Su, A. J. Thom, T. Tsuchimochi, V. Vanovschi, L. Vogt, O. Vydrov, T. Wang, M. A. Watson, J. Wenzel, A. White, C. F. Williams, J. Yang, S. Yeganeh, S. R. Yost, Z.-Q. You, I. Y. Zhang, X. Zhang, Y. Zhao, B. R. Brooks, G. K. Chan, D. M. Chipman, C. J. Cramer, W. A. Goddard, M. S. Gordon, W. J. Hehre, A. Klamt, H. F. Schaefer, M. W. Schmidt, C. D. Sherrill, D. G. Truhlar, A. Warshel, X. Xu, A. Aspuru-Guzik, R. Baer, A. T. Bell, N. A. Besley, J.-D. Chai, A. Dreuw, B. D. Dunietz, T. R. Furlani, S. R. Gwaltney, C.-P. Hsu, Y. Jung, J. Kong, D. S. Lambrecht, W. Liang, C. Ochsenfeld, V. A. Rassolov, L. V. Slipchenko, J. E. Subotnik, T. V. Voorhis, J. M. Herbert, A. I. Krylov, P. M. Gill and M. Head-Gordon, *Mol. Phys.*, 2014, **113**, 184–215.

41 S. Maeda, K. Ohno and K. Morokuma, *J. Chem. Theory Comput.*, 2010, **6**, 1538–1545.

42 X. Zhang and J. M. Herbert, *J. Phys. Chem. B*, 2014, **118**, 7806–7817.

43 S. Hirata and M. Head-Gordon, *Chem. Phys. Lett.*, 1999, **314**, 291–299.

44 M. A. Rohrdanz, K. M. Martins and J. M. Herbert, *J. Chem. Phys.*, 2009, **130**, 054112.

45 T. J. Penfold, *J. Phys. Chem. C*, 2015, **119**, 13535–13544.

46 E. Livshits and R. Baer, *Phys. Chem. Chem. Phys.*, 2007, **9**, 2932.

47 H. Sun, C. Zhong and J.-L. Brédas, *J. Chem. Theory Comput.*, 2015, **11**, 3851–3858.

48 J. Eng, B. Laidlaw and T. J. Penfold, *J. Comp. Chem.* https://doi.org/10.1002/jcc.25868 (2019).

49 R. Ditchfield, W. J. Hehre and J. A. Pople, *J. Chem. Phys.*, 1971, **54**, 724–728.

50 W. J. Hehre, R. Ditchfield and J. A. Pople, *J. Chem. Phys.*, 1972, **56**, 2257–2261.

51 P. Hariharan and J. Pople, *Mol. Phys.*, 1974, **27**, 209–214.

52 I. S. Ufimtsev and T. J. Martinez, *J. Chem. Theory Comput.*, 2009, **5**, 2619–2628.

53 J. P. Perdew and Y. Wang, *Phys. Rev. B*, 1992, **45**, 13244–13249.

54 J. P. Perdew, K. Burke and M. Ernzerhof, *Phys. Rev. Lett.*, 1996, **77**, 3865–3868.

55 J. S. Binkley, J. A. Pople and W. J. Hehre, *J. Am. Chem. Soc.*, 1980, **102**, 939–947.

56 M. S. Gordon, J. S. Binkley, J. A. Pople, W. J. Pietro and W. J. Hehre, *J. Am. Chem. Soc.*, 1982, **104**, 2797–2803.

57 L. Verlet, *Phys. Rev.*, 1967, **159**, 98.

58 J. Gibson and T. Penfold, *Phys. Chem. Chem. Phys.*, 2017, **19**, 8428–8434.

59 D. Wolfgang, K. Horst *et al.*, *Conical intersections: electronic structure, dynamics & spectroscopy*, World Scientific, 2004, vol. 15.

60 T. Penfold and G. Worth, *Chem. Phys.*, 2010, **375**, 58–66.

61 S. Aloïse, C. Ruckebusch, L. Blanchet, J. Réhault, G. Buntinx and J.-P. Huvenne, *J. Phys. Chem. A*, 2008, **112**, 224–231.

62 C. Sousa, C. de Graaf, A. Rudavskyi, R. Broer, J. Tatchen, M. Etinski and C. M. Marian, *Chem.: Eur. J.*, 2013, **19**, 17541–17551.

63 P. de Silva, C. A. Kim, T. Zhu and T. Van Voorhis, *ChemRxiv* 2019 doi.org/10.26434/chemrxiv.7854968.v1.

64 T. Hatakeyama, K. Shiren, K. Nakajima, S. Nomura, S. Nakatsuka, K. Kinoshita, J. Ni, Y. Ono and T. Ikuta, *Adv. Mater.*, 2016, **28**, 2777–2781.

65 T. Northey and T. Penfold, *Org. Electron.*, 2018, **12**, 1988–1991.

66 A. Pershin, D. Hall, V. Lemaur, J.-C. Sancho-Garcia, L. Muccioli, E. Zysman-Colman, D. Beljonne and Y. Olivier, *Nat. Comm.*, 2019, **10**, 597.